

# Transport and deposition of weakly inertial particles in closed channel flows at low Reynolds number

A. Hajjar<sup>\*</sup>, L. Scholtès, C. Oltéan, M.A. Buès

Université de Lorraine, CNRS, CREGU, GeoRessources UMR 7359, 54518 Vandoeuvre-lès-Nancy, France

## ARTICLE INFO

### Article history:

Received 22 December 2016

Received in revised form 14 May 2017

Accepted 19 May 2017

Available online 2 June 2017

### Keywords:

Particle-laden flows

Laminar flow

Particle trajectory

Transport

Deposition

Wavy channel

## ABSTRACT

An analytical approach is developed to show how particles sparsely distributed in steady and laminar channel flows can be transported for long distances or conversely deposited inside the channel due to the relative importance between the flow-induced drag and gravity forces. More precisely, we establish a rather simple particle trajectory equation which demonstrates that when particles' inertia is negligible, their behavior is characterized by the channel geometry and by a dimensionless number  $W$  that relates the ratio of the particles sedimentation terminal velocity to the flow mean velocity. The proposed particle trajectory equation is verified by comparing its predictions to particle tracking numerical simulations taking into account particle inertia and fully resolving equations. The equation is shown to be valid under the conditions that flow inertial effects are limited. Based on this trajectory equation, we build a regime diagram that can predict the behavior of particles entering closed channel flows. This diagram, by relating  $W$  to the ratio of the channel mean aperture to its total length, enables to forecast if the particles entering the flow will be either deposited or transported along the channel. The influence of the channel geometry on the particle behavior is then investigated by considering channels with straight and sinusoidal walls. In particular, the effect of the corrugation amplitude, of the asymmetry and of the phase lag between the walls on the extent of the transport and deposition zones is evaluated and verified against numerical experiments. Firstly, it is shown that the regime diagram for straight channels can be used for wavy channels with in-phase walls. Secondly, it is found that increasing the phase lag between the two walls and/or the walls corrugation amplitude leads to an increase of both the transport and sedimentation zones. Finally, it is demonstrated that increasing the lower wall corrugation amplitude relatively to the upper wall corrugation enhances particle transport.

© 2017 Elsevier Masson SAS. All rights reserved.

## 1. Introduction

Understanding the transport and deposition of inertial particles in channel flows is of fundamental importance in many environmental issues, such as underground pollution or fracture hydraulics, and in several industrial applications, like water filtration or mineral separation. The equation of motion for small rigid spherical particles in non-uniform unsteady flows at low Reynolds number was rigorously derived by Maxey and Riley [1] and Gatignol [2] who evaluated the forces acting on particles in a non-uniform flow field. In fact, when particle size and/or density are not negligible, the particle has a proper dynamic that differs from a tracer particle which follows perfectly the flow streamline. For instance, Stommel [3] studied particle motion in cellular flow fields without taking into account particle inertia, and the particle's trajectory was calculated according to the ratio between the

particle's settling velocity and the flow's vortex velocity. Maxey [4] extended the previous work to include the effect of particle inertia and found that two new dimensionless numbers must be considered: the Stokes number, which represents the ratio between the particle characteristic time and the flow characteristic time, and the particle to fluid density ratio. The experimental results by Bergounoux et al. [5] showed that the model proposed by Stommel could be valid for Stokes number up to 0.1.

The motion of inertial particles can be very complex even when particles are passive and have non-Brownian dynamics (Babiano et al. [6], Haller and Sapsis [7], Cartwright et al. [8], Balkovsky et al. [9]). This characteristic behavior of inertial particles was shown to have a great importance in many practical situations in Earth sciences like oceanology (Lunau et al. [10]) and atmospheric sciences (Shaw [11]). Another interesting feature of inertial particles is that under the effect of their inertia, they tend to accumulate in well defined regions of the flow. This phenomena has been widely studied for different types of fluid flows (for example, Eaton and Fessler [12] in turbulent flows, Bec [13] in random flows,

<sup>\*</sup> Corresponding author.

E-mail address: [ahmad.hajjar@univ-lorraine.fr](mailto:ahmad.hajjar@univ-lorraine.fr) (A. Hajjar).

Nizkaya et al. [14] in laminar flows, Angilella et al. [15] in vortex flows).

For particle motion in closed channel flows, most previous works focused on the phenomena of particle migration across the streamlines. It was found that both neutrally and non-neutrally buoyant particles can migrate across the streamlines to some equilibrium positions within the channel. For instance, Segre and Silberberg [16] observed by experiments that particles in a laminar pipe Poiseuille flow congregate at an annulus at 0.6 times of the pipe radius from the centerline of the pipe, a phenomena known as the tubular pinch effect. Since then, this phenomenon has been studied extensively using theoretical [Schonberg et al. [17], Asmolov [18]], experimental [Karnis et al. [19], Matas et al. [20]] and numerical approaches [Feng et al. [21], Yang et al. [22]] to better understand its physical mechanisms. This phenomena has important applications in inertial focusing and separation of particles in microfluidics (Di Carlo et al. [23], Martel and Toner [24]). In this case, the migration is due to the fluid inertia as it was theoretically demonstrated that lateral migration cannot occur under Stokes flow conditions (Bretherton [25], Ho and Leal [26]).

Taking into account particle inertia, Jebakumar et al. [27] investigated the effects of Stokes number on particle trajectories in wall-bounded vertical channel flow and found that for small Stokes number, particles behave similarly to neutrally buoyant particles. However, few works have investigated the effect of gravity on the motion of non neutrally buoyant particles in horizontal channel flows. For example, Chen et al. [28,29] studied the deposition of charged particles in straight and convergent channels, investigating the contribution of gravity and image forces in the particle deposition process. Even less works considered particle transport and deposition in channels with wavy walls. For instance, based on migration conditions formulated initially by Sapsis and Haller [30], Nizkaya et al. [14] neglected fluid inertia and studied particle focusing in channels with periodic corrugated walls. In particular, they showed that, even if the fluid inertial effects are neglected, focusing can occur due to particle inertia and to the waviness of the streamlines imposed by walls corrugation. They also defined a trapping diagram that predicts the presence of inertial focusing as a function of the channel geometry and of the flow Froude number.

In the present work, our aim is to study the transport and deposition of non-Brownian small spherical particles immersed in closed channel flows, by calculating the well-defined particle trajectories. Particle inertia, which is defined by the particle response time, is so weak that the focusing phenomenon observed in [14] is not expected to occur. The flow in the channel is assumed to be steady and to follow the local cubic law (LCL), which is an analytical solution of Stokes equations for flow motion within thin channels (Zimmerman and Bodvarsson [31]). The flow is thus unidirectional and laminar. In addition, we make the assumption that the particles are sparsely distributed inside the fluid so that the flow affects the motion of the particles, but not vice versa. In other words, we thus consider here only a one way coupling between the solid and fluid phases.

The paper is organized as follows. In Section 2, we develop the equations of the particle trajectories in fluid flows in both straight and wavy channels. In Section 3, we verify these equations through numerical simulations using a hybrid technique with the combination of a finite element method and a Lagrangian particle tracking method. In Section 4, we establish the diagrams defining different particle transport regimes and demonstrate their validity by comparing their predictions against numerical experiments. In Section 5, we conclude and present some directions of future work.

## 2. Governing equations

We consider 2D flows. The domain is represented in a reference frame  $(X, Z)$  where  $X$  corresponds to the horizontal direction (the main flow direction) and  $Z$  to the vertical one. Gravity is taken into account and applies perpendicularly to the main flow direction (along  $Z$ ).

### 2.1. Particle motion equation and particle trajectory equation

When the particle diameter is small and when the Reynolds number as well as the velocity gradients around the particle are small, the equation of motion of a solid spherical particle of radius  $a$  and density  $\rho_p$  moving in a fluid of density  $\rho_f$  and dynamic viscosity  $\mu$ , as derived [1], with corrected added mass term (Auton et al. [32]) can be written as:

$$m_p \frac{d\vec{V}_p}{dt} = (m_p - m_f) \vec{g} \quad \text{gravity and buoyancy forces}$$

$$- \frac{m_f}{2} \left[ \frac{d\vec{V}_p}{dt} - \frac{D}{Dt} \left( \vec{V}_f + \frac{a^2}{10} \nabla^2 \vec{V}_f \right) \right] \quad \text{added mass contribution}$$

$$+ m_f \frac{D\vec{V}_f}{Dt} \quad \text{unperturbed flow pressure gradient}$$

$$- 6\pi a \mu \left( \vec{V}_p - \vec{V}_f - \frac{a^2}{6} \nabla^2 \vec{V}_f \right) \quad \text{drag force}$$

$$- 6\pi a^2 \mu \int_{-\infty}^t \frac{1}{\sqrt{\pi(t-t')}} \frac{d}{dt'} \left[ \vec{V}_p - \vec{V}_f - \frac{a^2}{6} \nabla^2 \vec{V}_f \right] dt' \quad \text{Basset history force}$$

$$(1)$$

where  $\vec{V}_p$  is the particle velocity,  $\vec{V}_f$  is the fluid velocity,  $m_p = \frac{4}{3}\pi\rho_p a^3$  is the particle mass,  $m_f = \frac{4}{3}\pi\rho_f a^3$  is the mass of the displaced fluid and  $\vec{g}$  is the gravity field vector.  $\frac{d}{dt}$  denotes the derivative with respect to time taken along the particle trajectory and  $\frac{D}{Dt}$  denotes the derivative taken along the path of a fluid element. The forces taken into account in this equation, in their order of appearance, are: gravity and buoyancy forces, added mass contribution, force due to the pressure gradient of the unperturbed flow, drag force, and Basset history force due to unsteadiness of the disturbance flow around the particle, which reflects the impact of the delay caused by viscous diffusion of momentum between the surface of the particle and the flow (Druzhinin and Ostrovsky [33]). We assume that the characteristic time of the momentum diffusion is very small so that the this disturbance flow is quasi-steady around the particle and Basset force can be neglected. The terms proportional to the Laplacian of the velocity field, known as Faxen corrections [34], are due to the non-uniformity of the fluid flow at the particle scale. They can be neglected under the assumption that the particle radius is substantially small compared to the characteristic length  $L_0$  of the flow. In Eq. (1), the lift forces are not taken into account because the effects of fluid inertia leading to these forces are neglected.

Under these conditions, i.e. neglecting Basset force and Faxen corrections terms, and developing the terms of the right-hand side of Eq. (1), we can write:

$$\frac{L_0}{V_0} \frac{d\vec{V}_p}{dt} = \frac{1}{\tau} \left( \vec{V}_f - \vec{V}_p + \frac{2}{9} \frac{a^2(1-k)g}{\nu} \frac{\vec{g}}{|g|} \right) + \frac{L_0}{V_0} \frac{3R}{2} \frac{D}{Dt} (\vec{V}_f) \quad (2)$$

where  $\tau = \frac{2}{9R} \frac{a^2 V_0}{\nu L_0} = \frac{St}{R}$  represents the particle dimensionless response time,  $St$  being the Stokes number and  $R = \frac{2\rho_f}{2\rho_p + \rho_f} = \frac{2}{2k+1}$

a dimensionless number where  $k = \frac{\rho_p}{\rho_f}$  is the ratio of particle density to fluid density,  $V_0$  is the flow mean velocity and  $\nu$  is the fluid kinematic viscosity. Particle inertia is characterized by its response time  $\tau$ , defined as the ratio between the particle characteristic time (particle relaxation time) and the flow characteristic time  $T_0 = \frac{L_0}{V_0}$ . We consider the case of low particle inertia for which  $\tau \ll 1$ . In this case, the term proportional to  $1/\tau$  is dominant in Eq. (2) compared to the two other terms, and Eq. (2) can thus be simplified to:

$$\vec{V}_p = \vec{V}_f + \frac{2}{9} \frac{a^2(k-1)g}{\nu} \frac{\vec{g}}{|g|} \quad (3)$$

where  $\frac{\vec{g}}{|g|}$  is a vertical unit vector pointing in the downward direction. This equation corresponds to inertia-free sedimenting particles and has been already used in the past (e.g. [3,5]).

According to Eq. (3), in 2D, the two components of the particle velocity are thus:

$$V_p^x = V_f^x = \frac{dX_p}{dt} \quad \text{and} \quad V_p^z = V_f^z + \frac{2}{9} \frac{a^2(1-k)g}{\nu} = \frac{dZ_p}{dt} \quad (4)$$

where  $X_p$  and  $Z_p$  are the particle coordinates. This equation shows that neutrally buoyant inertia-free particles ( $k = 1$  and  $\tau \rightarrow 0$ ) follow exactly the flow streamlines. For heavy particles (denser than the fluid such as  $k > 1$ ),  $V_p^z < V_f^z$ , and for particles lighter than the fluid such as  $k < 1$ ,  $V_p^z > V_f^z$ . For the general case, the trajectory of the particle is then defined by:

$$\frac{dZ_p}{dX_p} = \frac{dZ_p}{dt} \frac{dt}{dX_p} = \frac{V_f^z + \frac{2}{9} \frac{a^2(1-k)g}{\nu}}{V_f^x}. \quad (5)$$

Choosing  $L_\infty$  and  $H_0$  as length scales and  $V_0$  as a velocity scale, the following dimensionless parameters are defined:

$$h^* = \frac{H_0}{L_\infty}, x = \frac{X}{L_\infty}, z = \frac{Z}{H_0}, v_f^x = \frac{V_f^x}{V_0} \quad \text{and} \quad v_f^z = \frac{1}{h^*} \frac{V_f^z}{V_0}.$$

Eq. (5) can then be rewritten in the dimensionless form:

$$\frac{dz_p}{dx_p} = \frac{dz_p}{dt} \frac{dt}{dx_p} = \frac{v_f^z - \frac{W}{h^*}}{v_f^x} \quad (6)$$

where  $W = \frac{2}{9} \frac{a^2(k-1)g}{\nu V_0}$  is a dimensionless number that represents the ratio between the particle sedimentation Stokes velocity and the flow mean velocity.

Knowing the particle initial position  $(x_p^0, z_p^0)$ , and knowing the components of the fluid velocity at each point  $(x, z)$  the integration of Eq. (6) enables to find the position of the particle according to the velocity components of the fluid. In the next section,  $\vec{v}_f$  will be calculated for a closed channel flow, assuming that the flow follows the local cubic law.

## 2.2. Local cubic law flow in a closed channel

We consider a 2D closed channel defined by the domain:  $D = \{(X, Z); X \in [0, L_\infty]; Z \in [\Phi_1(X), \Phi_2(X)]\}$  where  $\Phi_1(X)$  and  $\Phi_2(X)$  define periodic wall shapes. The geometry of a schematic channel is shown in Fig. 1. The total length of the channel is  $L_\infty$ , the amplitudes of the lower and higher walls are respectively  $A_1$  and  $A_2$ , and the wavelength of the walls of the channel is  $L_0$ . In addition, the microscopic roughness is neglected and the walls slopes  $|\partial\Phi_1/\partial X|$  and  $|\partial\Phi_2/\partial X|$  are smooth and small.

The mean aperture of the channel can be computed as  $H_0 = \frac{1}{L_\infty} \int_0^{L_\infty} (\Phi_2(X) - \Phi_1(X)) dX$ . The local half aperture at a point of coordinate  $X$  is equal to  $H(X) = \frac{1}{2}(\Phi_2(X) - \Phi_1(X))$  and the channel middle line equation is  $\Phi(X) = \frac{1}{2}(\Phi_1(X) + \Phi_2(X))$ . Following [31] and [14], using the dimensionless channel middle line  $\phi(x) = \frac{\Phi(X)}{H_0}$  and the dimensionless local half aperture  $h(x) = \frac{H(X)}{H_0}$ , we introduce

the cross channel coordinate defined by  $\eta = \frac{z - \phi(x)}{h(x)} \in [-1, 1]$  and the aspect ratio of the channel  $\epsilon = \frac{H_0}{L_0}$ . In the present study, we assume that  $\epsilon$  is small and that the flow is within a Stokes regime so that the fluid inertia can be safely neglected. This assumption is valid for small  $\epsilon Re_H$ , with  $Re_H = \frac{V_0 H_0}{\nu}$  the flow Reynolds number [31]. Under these assumptions, the flow is of Poiseuille type and is described by the local cubic law (LCL). The cubic law is an analytical solution of Navier–Stokes equations for a steady laminar flow between two planar surfaces. By applying Reynolds equation on the local aperture level (Mourzenko et al. [35]) and using a harmonic averaged aperture, neglecting fluid inertia and assuming  $\epsilon \ll 1$ , the cubic law holds locally and can be generalized to the LCL that can thus be used to describe flow in a wavy periodic channel, such as:

$$\frac{\Delta P}{L_\infty} = \frac{-12\mu Q}{H_h^3} \quad (7)$$

where  $\Delta P$  is the pressure difference along the flow direction,  $H_h = 2H_0(\langle h^{-3} \rangle)^{-1/3}$  is the hydraulic aperture, with  $\langle h^{-3} \rangle = \frac{H_0^3}{L_\infty} \int_0^{L_\infty} \frac{dX}{H^3(X)}$  being the dimensionless hydraulic or apparent aperture of the channel and  $Q = \int_{\Phi_1(X)}^{\Phi_2(X)} V_x(X, Z) dZ$  is the volumetric flow rate per unit length. The mean velocity of the flow is  $V_0 = Q/H_0$ .

Under the LCL assumption, the components of the fluid flow velocity vector, expressed in  $(x, \eta)$  coordinates, are equal to [31,14]:

$$v_f^x = \frac{3}{4h(x)}(1 - \eta^2) \quad \text{and} \quad v_f^z = \frac{3(\phi'(x) + \eta h'(x))}{4h(x)}(1 - \eta^2) \quad (8)$$

where  $h'(x)$  and  $\phi'(x)$  correspond respectively to the variations of the dimensionless channel aperture and channel middle line along the flow direction.

## 2.3. Particle trajectory equation in closed channel flow

Using Eqs. (6) and (8), the trajectory of an inertia-free particle in a closed channel LCL flow can be defined by:

$$\frac{dz_p}{dx_p} = \frac{-4h(x)}{3(1 - \eta^2)} \frac{W}{h^*} + (\phi'(x) + \eta h'(x)). \quad (9)$$

The trajectory of the particle thus depends on the channel geometrical parameters  $h(X)$  and  $\phi(X)$ , and on the ratio  $\frac{W}{h^*}$ .

Eq. (9) can then be used to determine particle trajectories in straight channels and in channels with sinusoidal walls.

### 2.3.1. Straight channel

We consider the simple case of a horizontal channel of total length  $L_\infty$  constituted by two parallel straight walls. The aperture between the walls is  $H_0$ . In this case,  $\phi_1(x) = -1/2$ ,  $\phi_2(x) = 1/2$ ,  $h(x) = 1/2$ ,  $\phi(x) = 0$ ,  $h'(x) = \phi'(x) = 0$ ,  $\eta = 2z$ , and Eq. (7) becomes:

$$\frac{dz_p}{dx_p} = \frac{-2}{3(1 - 4z^2)} \frac{W}{h^*}. \quad (10)$$

Integrating Eq. (10) between the initial position of the particle  $(x_p^0, z_p^0)$  and its actual position  $(x_p, z_p)$ , the equation of the particle trajectory in a straight channel is finally given by:

$$3(z_p - z_p^0) - 4(z_p^3 - (z_p^0)^3) = 2 \frac{W}{h^*} (x_p^0 - x_p). \quad (11)$$

Eq. (11) enables to predict the final position of a particle injected at a defined initial position inside the channel, and in particular allows to know if the particle will settle inside the channel or if it will be transported till the outlet. This can be done by replacing  $x_p$  by 1 (which corresponds to  $x_p = L_\infty$ ) and by searching for the corresponding  $z_p$ . If  $z_p > -\frac{1}{2}$ , the particle will exit the channel, and if  $z_p < -\frac{1}{2}$  the particle will settle inside.

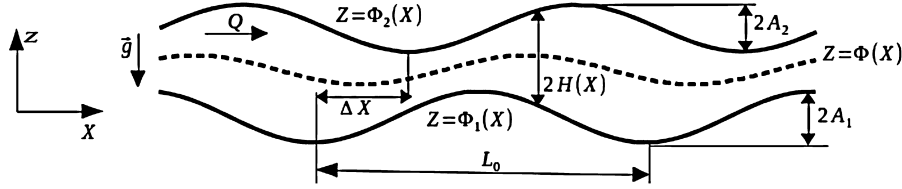


Fig. 1. 2D closed channel with wavy periodic walls.

### 2.3.2. Wavy channel with sinusoidal walls

For the case of a channel with sinusoidal walls, the walls are defined by :

$$\begin{aligned}\Phi_1(X) &= \frac{H_0}{2} + A_1 \sin\left(\frac{2\pi}{L_0}\left(X - \frac{\Delta X}{2}\right)\right) \quad \text{and} \\ \Phi_2(X) &= \frac{H_0}{2} + A_2 \sin\left(\frac{2\pi}{L_0}\left(X + \frac{\Delta X}{2}\right)\right)\end{aligned}\quad (12)$$

where  $A_1$  is the lower wall amplitude,  $A_2$  is the upper wall amplitude, and  $\Delta X$  is the horizontal shift between the two walls (Fig. 1). In this case, the expressions of the dimensionless local aperture and channel middle line and their derivatives are more complex so an equation in the form of Eq. (11) is difficult to obtain analytically. Nonetheless, it is possible to find the position of a particle by numerically integrating Eq. (5) over  $[x_p^0, 1]$  considering  $z(x_p^0) = z_p^0$  as the initial condition. For the simple case of channels having two parallel walls, making the substitution  $z^*(x) = z(x) - \phi(x)$  leads to an equation relating  $z^*(x)$  and  $x$  identical to Eq. (10). Therefore, the behavior of particles transported in wavy channels with parallel walls is identical to the one occurring in straight channels, when studied with the channel middle line as reference.

## 3. Numerical verification

In this section, we verify Eqs. (9) and (11) by performing numerical simulations. These equations were developed under the assumption that particle inertia can be neglected (Eq. (3)) and the flow velocity components were calculated using the LCL which assumes that the flow is dominated by viscous forces. The numerical simulations presented here aim to test the validity of these assumptions and to verify Eqs. (9) and (11) by taking into account particle inertia and fully resolving the continuity and Navier–Stokes equations governing the fluid flow inside the channel.

Finite Element Method is used to solve the flow equations and a Lagrangian Tracking technique is used to track the particles motion in the flow by integrating the particles motion equation (Eq. (2)). For each particle, an ordinary differential equation is solved for each position vector component (2 equations are solved in 2D) using the finite Difference Method. At each time step, the forces acting on each particle are obtained from the calculated fields at the current particle position. Particles positions are then updated. This process is repeated until the preset simulation time is reached or when the particle comes into contact with a boundary.

The ordinary differential equation used in the simulations is Eq. (2), which corresponds to Eq. (1), where Faxen corrections and Basset history force are neglected under the assumptions that particle size is small compared to the channel aperture and that the disturbance flow due to the particle is quasi-steady.

### 3.1. Simulation procedure

- The geometry of the channel is first defined. In the case of a straight channel, it is represented by a horizontal rectangle defined by the channel aperture as its width and the channel total length as its length. In the case of a channel with sinusoidal walls, the two walls are constructed according to

the expressions of  $\Phi_1(X)$  and  $\Phi_2(X)$  (see Section 2.3.2). The channel is then built by defining its mean aperture and the horizontal shift. The channel inlet consists of a square part.

- The computational domain is discretized by using triangular meshes (Fig. 2). The mesh is refined in the near wall regions and gradually coarsened when moving towards the channel center. A grid independence test has been performed to determine the optimal number of elements. For example, on a total meshed area of 0.0049 m<sup>2</sup>, the average element surface area is 0.0192 mm<sup>2</sup>. The mesh chosen for this case consists of 252364 elements.
- A parabolic velocity profile with a mean flow velocity  $V_0$  is defined at the inlet, a zero pressure is imposed at the outlet  $P_{outlet} = 0$  (Fig. 2), and the no-slip boundary conditions are imposed on the channel walls ( $V_f = 0$ ).
- The continuity and Navier–Stokes equations governing the steady incompressible flow in the channel are solved, and the pressure and velocity fields are computed. In this case, the continuity equation that represents the conservation of mass reads as:

$$\nabla \cdot \vec{V}_f = 0 \quad (13)$$

and the equation of Navier–Stokes that express the conservation of momentum are written as:

$$\rho_f((\vec{V}_f \cdot \nabla) \vec{V}_f) = \rho_f \vec{g} - \nabla P + \mu \nabla^2 \vec{V}_f. \quad (14)$$

- The properties of the particles (density and diameter) and their number are determined based on the value of  $W$  (see Section 2.3). The particles are then released with zero initial velocity at  $X = 0$  and at different vertical positions.
- The last step of the simulation consists in calculating the particle trajectories by solving the equation of motion for each particle (Eq. (2)). When a particle comes into contact with a wall, it sticks to it and it is considered as deposited. The calculation of its trajectory is then terminated.

## 3.2. Results

### 3.2.1. Flow in wavy channels

#### a. Unidirectional flow and appearance of recirculation zones

Eq. (9) was established assuming that the flow is laminar. However, it has been shown that recirculation zones could appear in the cavities of wavy channels even at low Reynolds number (e.g. Sisavath et al. [36]). To find the critical value of  $\epsilon Re_H$  below which these inertial effects can be neglected, we performed several simulations and found that the flow is more likely to present recirculation zones in channel with mirror symmetric walls ( $\Delta X/L_0 = 0.5$ ). More particularly, in this configuration, recirculation zones begin to appear when  $\epsilon Re_H > 10$ . On the other hand, in channel with parallel walls ( $\Delta X/L_0 = 0$ ), recirculations begin to appear when  $\epsilon Re_H > 100$  (Fig. 3).

With regard to these results,  $\epsilon Re_H$  was kept lower than 10 to make sure that no recirculation zones appear in all the geometries considered in the present study. In this case, flow inertial effects



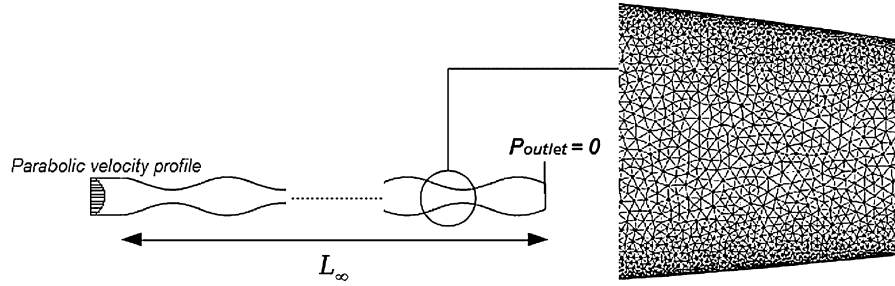


**Fig. 2.** Boundary conditions applied on a channel with sinusoidal walls (left) and the grid consisting of triangular meshes (right) used in the numerical simulations.

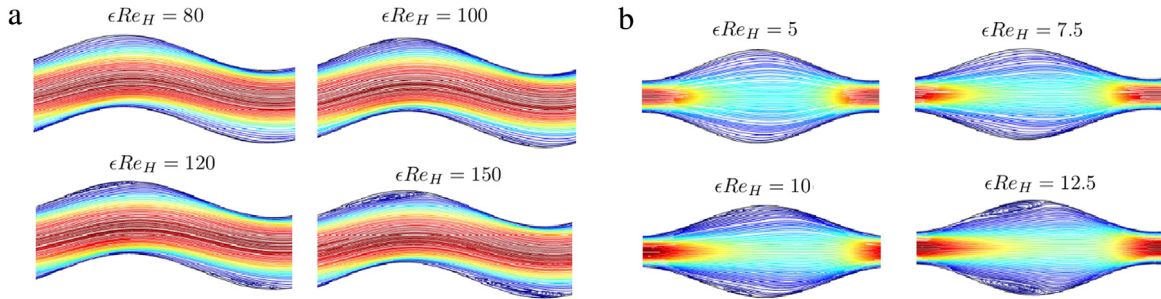


**Fig. 3.** Flow streamlines in channels with in phase walls (a) and mirror symmetric walls (b) for different values of  $\epsilon Re_H$ . Red streamlines correspond to high velocity magnitudes while blue ones correspond to low velocity magnitudes. (For interpretation of the references to color in this figure legend, the reader is referred to the web version of this article.)

were assumed to be sufficiently small for the LCL to be valid. However, the validity of this assumption can vary according to the channel geometry as discussed in the following subsection.

#### b. Validity range of the Local cubic law

To further study the validity of the LCL, the velocity profiles computed from Navier–Stokes (NS) equation were compared to the LCL solution (Eq. (8)) for  $\epsilon Re_H = 7$  for a channel with parallel walls and a channel with mirror symmetric walls. The velocity profiles were computed along two cutlines located respectively at  $X = 2 * L_0$  and  $X = 2.5 * L_0$  (Fig. 2) and are presented in Fig. 4.

One can see that the NS and LCL solutions coincide exactly when the channel walls are parallel whereas the two profiles deviate slightly in the channel with mirror symmetric walls. This result confirms the validity of the LCL for low  $\epsilon Re_H$ , and it also shows that this validity can be nonetheless moderately affected by the channel geometry.

### 3.2.2. Particle trajectories

#### a. Straight channel

To verify Eq. (11), we computed numerically the trajectories of particles in a straight channel considering the full equation (Eq. (2)). We set up a numerical experiment with a channel of total length  $L_\infty = 1$  m and of aperture  $H_0 = 5$  mm. 5 particles of radius  $a = 5 \mu\text{m}$  and density ratio  $k = 2.5$  were injected in the channel at the same initial horizontal position  $x_p^0$  but at different initial vertical positions  $z_p^0$ . Water was used as a fluid and the mean flow velocity  $V_0$  was fixed equal to 0.01 m/s. In this case  $W = 0.00817$  and  $\tau = 1.66 * 10^{-7}$ . The final distance  $x_p^f$  traveled by each particle until they come in contact with the bottom wall was calculated for each particle initial vertical position  $z_p^0$  and comparisons were made with respect to the predictions of Eq. (11). As shown in Fig. 5, the two approaches are in very good agreement with a maximum relative error between the predicted final particle positions equal to 0.2%.

#### b. Wavy channel

To verify Eq. (9) for the case of wavy channels, we considered a channel defined by two sinusoidal walls with  $H_0 = 5$  mm,

$L_0 = 5$  cm,  $L_\infty = 0.98$  m,  $A_1 = 1.5$  mm,  $A_2 = 2$  mm, and  $\Delta X = 0.25 L_0$  (Fig. 1). This case corresponds to a general case of a random geometry because the channel walls are neither identical nor parallel. The particle properties and initial positions were chosen equal to the ones used in the previous section (straight channel case) and the flow mean velocity was also fixed equal to  $V_0 = 0.01$  m/s. In this case  $W = 0.00817$  and  $\tau = 3.33 * 10^{-6}$ . The distances  $x_p^f$  traveled by the particle for different initial vertical positions  $z_p^0$  are plotted in Fig. 6, for both solutions given by Eq. (9) and by the numerical model. The two approaches are here again in good agreement with a maximum relative error of about 3.3% between their respective predictions. The origin of this relative error is investigated in Section 3.2.2.d.

#### c. Dependence of the particle trajectory on $W$

In the two previous sections, we verified the particle trajectory equations in straight and wavy channels for specific geometries. However, according to Eq. (9), the trajectory depends on the geometry of the channel ( $\phi'(x)$  and  $h'(x)$ ) and the ratio  $\frac{W}{h^*}$ . For a specified channel geometry ( $h^*$  is constant),  $W$  is the only dimensionless parameter affecting particle trajectories. More precisely, if, in the same channel, two particles with different properties are injected in two flows with different characteristics (velocity, viscosity), the particles should follow the same trajectory if they present the same dimensionless number  $W$ , which depends on the particle properties and on the flow characteristics.

In order to verify the dependency of particle trajectories on  $W$ , we conducted a sensitivity analysis. To do so, we first studied 5 cases (cases 1 to 5 in Table 1) in which the particle properties and fluid mean velocities were different but  $W$  was kept quasi constant ( $\approx 0.0043$ ). For each case, 8 particles were injected in the channel at different initial vertical positions  $z_p^0$ . The distances  $x_p^f$  traveled by the particles are plotted in Fig. 7 as a function of their initial positions for different initial vertical positions. The maximum relative error between the numerical and the analytical solutions of the distances traveled by the particles is 5.1%. Nonetheless, in all cases, particles injected at the same initial altitude travel approximately the same distance before sedimentation, if  $W$  is kept constant.

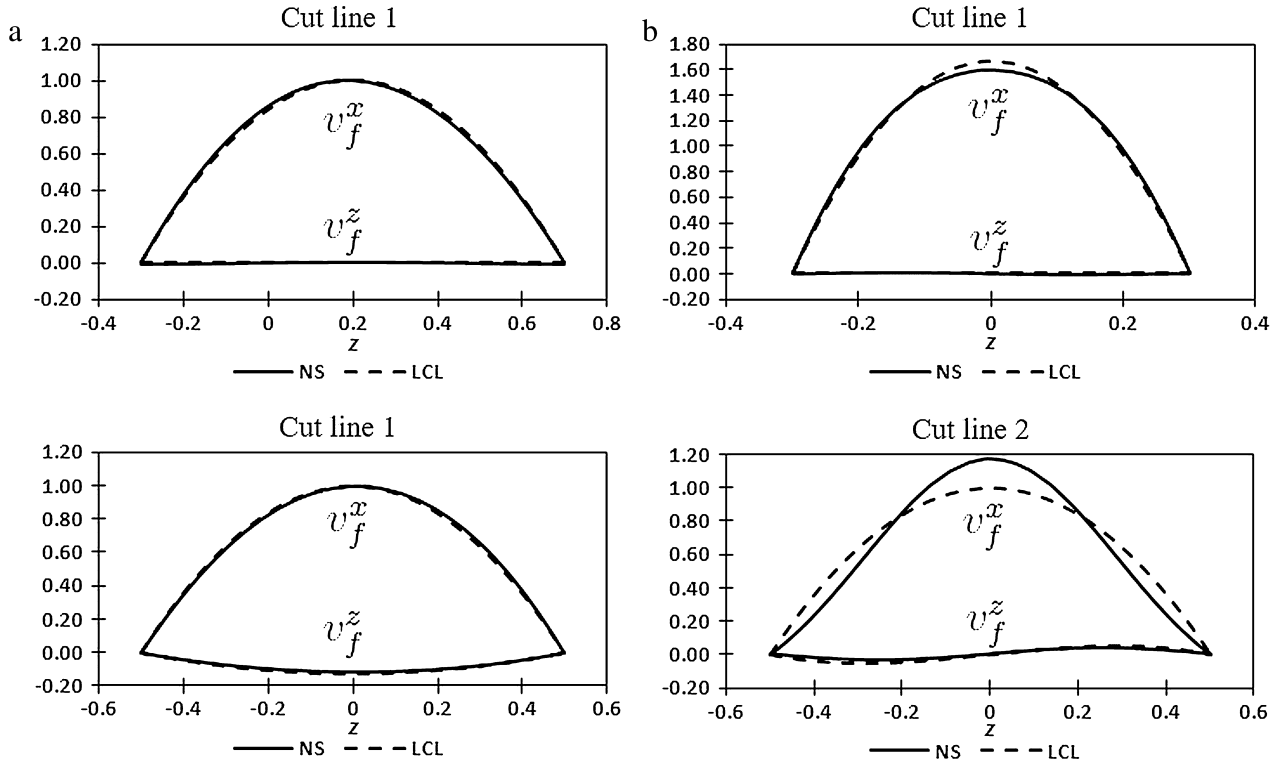


**Fig. 4.** Velocity profiles for  $\epsilon Re_H = 7$  in channels with parallel walls (a) and mirror symmetric walls (b). Comparison of the LCL solution and Navier–Stokes numerical solution.

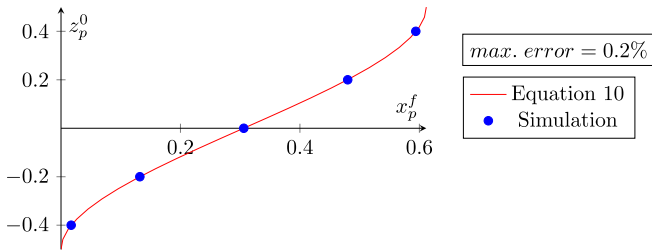


**Fig. 5.** Distances  $x_p^f$  traveled by particles with different initial vertical positions  $z_p^0$  in a straight channel such as  $W = 0.00817$  and  $\tau = 1.66 \times 10^{-7}$ . Comparison between Eq. (11) (solid line) and particle tracking numerical simulations (symbols).

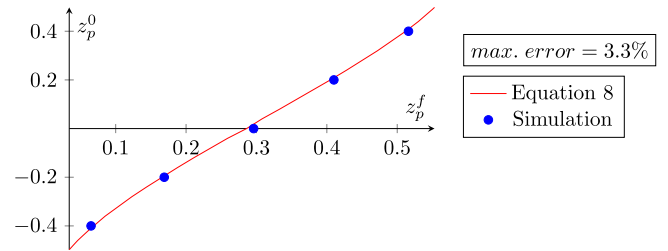


**Fig. 6.** Distances  $x_p^f$  traveled by particles with different initial vertical position  $z_p^0$  in a wavy channel such as  $W = 0.00817$  and  $\tau = 3.33 \times 10^{-6}$ . Comparison between Eq. (9) (solid line) and particle tracking numerical simulations (symbols).

To further verify this dependency on  $W$ , 5 additional cases (cases 6 to 10 in Table 1) were tested for a value of  $W \approx 0.0081$ . The results of this second series of tests are plotted in Fig. 8. Here again, the dependency of particle trajectory on  $W$  in the non inertial regime is verified, validating furthermore its ability for determining particles' behavior in channel flows.

#### d. Relative error between the numerical and analytical solutions

The error between the numerical and analytical solutions can be due to: (i) errors in the numerical simulations, (ii) the assumptions under which the analytical model was developed such as the use of the LCL as a solution of Navier–Stokes equation or, (iii) the negligence of particle inertia. To investigate the origin of this error, the numerical solution of case 5, where the maximum relative error is equal to 5.11%, was recalculated 4 times under different conditions. The outcomes of this series of tests are as follows:

- When the mesh size is reduced by half, the maximum relative error remains equal to 5.11%.
- When the time step used to update the particle position is reduced by a factor of 2, the maximum relative error remains equal to 5.11%.

- When the particle inertia is neglected, the maximum relative error decreases slightly to 5%.
- When the Stokes equation is solved instead of Navier–Stokes equation (to neglect fluid inertia), the maximum relative error decreases to 4.08%.

Taking into account these results, it is clear that the numerical errors are limited since the relative error between the two solutions keeps similar whatever the mesh or time step refinement. On the other hand, neglecting particle and fluid inertia seems to reduce the relative error between the two approaches. According to Section 3.2.1, we can certainly argue that the error is due to the use of the LCL in Eq. (9) as it cannot ensure a perfect representation of the velocity field. Nonetheless, the error keeps limited if  $\epsilon Re_H$  remains small.

#### 4. Particle transport regimes diagrams

As illustrated in the previous section, the trajectories of small particles with very small inertia, in channel flows satisfying the LCL approximation, depend on the channel geometry and on the

**Table 1**

Flow characteristics and particles properties used in the simulation to ensure  $W \simeq 0.0043$  (cases 1 to 5) and  $W \simeq 0.00809$  (cases 6 to 10).

Parameter	$W$	$\tau$	$\epsilon Re_H$	$a(\mu m)$	$k$	$V_0$ (m/s)
Case 1	0.0043	$4.26 * 10^{-7}$	2.5	2.5	2.58	0.005
Case 2	0.00429	$1.89 * 10^{-6}$	4	5	1.63	0.008
Case 3	0.00431	$1.55 * 10^{-7}$	1	3	1.44	0.002
Case 4	0.00429	$4.62 * 10^{-6}$	5	7.5	1.35	0.01
Case 5	0.00432	$1.8 * 10^{-5}$	10	10.5	1.36	0.02
Case 6	0.00809	$5.35 * 10^{-7}$	1.5	4.5	1.55	0.003
Case 7	0.00809	$9.45 * 10^{-7}$	2.5	4	2.16	0.005
Case 8	0.00809	$6.97 * 10^{-6}$	3.75	11	1.23	0.0075
Case 9	0.00809	$7.07 * 10^{-6}$	7.5	8	1.87	0.015
Case 10	0.00809	$1.47 * 10^{-5}$	10	7	2.59	0.021

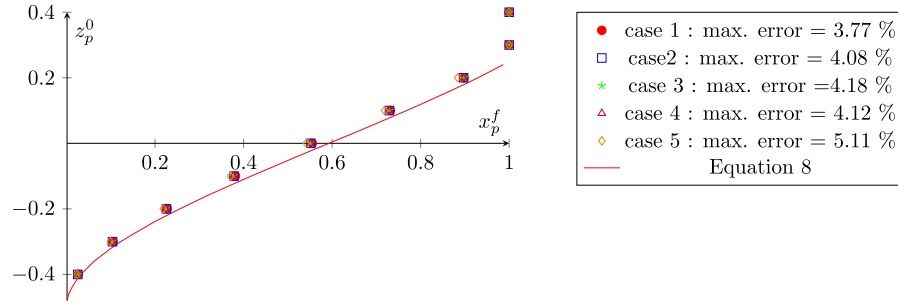


**Fig. 7.** Distances  $x_p^f$  traveled by particles with different initial positions  $z_p^0$  for different configurations presenting same  $W \simeq 0.004$ . Comparison between Eq. (9) (solid line) and particle tracking numerical simulations (symbols).

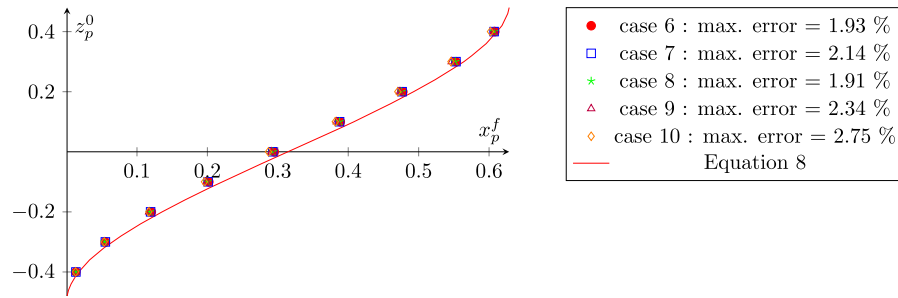


**Fig. 8.** Distances  $x_p^f$  traveled by particles with different initial positions  $z_p^0$  for different configurations presenting same  $W \simeq 0.0081$ . Comparison between Eq. (9) (solid line) and particle tracking numerical simulations (symbols).

dimensionless number  $W$ . In this section, we try to characterize the different transport regimes of these particles. To do so, we assume a uniform distribution of the particles at the inlet, and we start by defining three arbitrary regimes that can occur based on the amount of particles that settle inside the channel:

- **Transport:** At least 75% of the particles are transported in the channel till the outlet. All the particles having an initial vertical position  $z_p^0 \in [-1/4, 1/2[$  are transported till the outlet of the channel, and particles with  $z_p^0 \in ]-1/2, -1/4]$  settle inside the channel.
- **Sedimentation:** Assuming a uniform distribution of particles at the inlet, at least 75% of the particles settle inside the channel. Particles with  $z_p^0 \in ]1/4, 1/2[$  exit the channel, and the ones with  $z_p^0 \in ]-1/2, 1/4]$  settle inside the channel.
- **Transition:** Less than 75% but more than 25% of the particles exit the channel. This regime describes the transition between the transport and the sedimentation regimes described previously.

The arbitrary selection of the separating percentages 25% and 75% defining the transport regime will be discussed later on. The dependence of these different regimes on  $W$  is studied first in a

straight channel, and then in wavy channels with different geometrical properties (wavelength, amplitude, walls horizontal shift).

#### 4.1. Straight channel

The channel geometry is defined by the dimensionless parameter  $h^* = \frac{H_0}{L_\infty}$ . Based on Eq. (11), the three arbitrary regimes defined previously correspond respectively to different values of  $\frac{W}{h^*}$ :

- Transport:  $\frac{W}{h^*} < 0.156 = \frac{W_{cr1}}{h^*}$
- Sedimentation:  $\frac{W}{h^*} > 0.84 = \frac{W_{cr2}}{h^*}$
- Transition:  $0.156 < \frac{W}{h^*} < 0.84$

where  $W_{cr1}$  and  $W_{cr2}$  are critical values of  $W$  characterizing the transition between the different regimes.  $W_{cr1}$  and  $W_{cr2}$  vary linearly as a function of  $h^*$ . A diagram of transport regimes can then be established for straight channels as illustrated in Fig. 9. In Fig. 9(a), a 2D diagram is built where three different zones corresponding to the transport, transition and sedimentation zones are delimited by the linear variation of  $W_{cr1}$  and  $W_{cr2}$  as functions of  $h^*$ . In Fig. 9(b), a 1D diagram is built where these zones are presented according to the single parameter  $\frac{W}{h^*}$ . Although the 1D representation could be considered more relevant in terms of delimitation

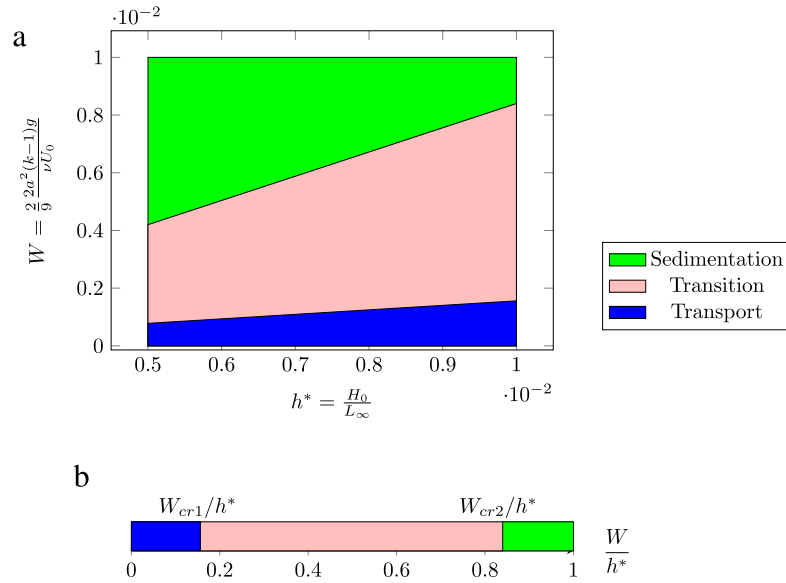


**Fig. 9.** Transport regimes diagram for weakly inertial particles in a closed straight channel flow. (a) 2D diagram representing the different zones according to the variation of  $W$  as a function of  $h^*$ . (b) 1D diagram representing these zones according to the parameter  $\frac{W}{h^*}$ .

of the three zones than the 2D one, it does not reflect clearly the respective contribution of parameters  $W$  and  $h^*$  on the variation of the regimes zones in the diagram. Consequently, we will keep the 2D representation along the paper as it gives a better graphical representation of the effects of either the channel geometry ( $h^*$ ) or the particle and flow properties  $W$  on the transport regimes. It will enable us subsequently to highlight the effects of the geometrical parameters of the channel on the variation of the different zones in the regime diagram. The 2D diagram represents the effects of the particle properties and the flow characteristics (represented by  $W$ ) as well as the effect of the channel geometry (represented by  $h^*$ ). Similar diagrams will be plotted subsequently to study the effect of the channel geometrical parameters on the transport regimes.

The particle transport regimes were arbitrarily defined so that the diagram depends on the percentages of particles that can be transported or deposited inside the channel. When changing these percentages, the variation of  $W_{cr1}$  and  $W_{cr2}$  as functions of  $h^*$  remains constant so that the regimes diagram keeps the same form but the transport and sedimentation zones will be wider or narrower. The variation of the ratios  $W_{cr1}/h^*$  and  $W_{cr2}/h^*$  as functions of the percentages of particles transported or sedimented is plotted in Fig. 10.

The critical ratio  $W_{cr2}/h^*$  increases when the arbitrary sedimentation regime is defined by a higher fraction of transported particles. Inversely,  $W_{cr1}/h^*$  decreases when the fraction of transported particles defining the arbitrary transport regime is bigger.

To verify numerically the regime diagram obtained for straight channels, a numerical experiment was conducted using the same particle tracking technique presented in Section 3, consisting this time in injecting 100 particles near the channel inlet for three different values of the pair  $(h^*, W)$ . These three values correspond respectively to configurations located in the transport ( $h^* = 0.008$ ,  $W = 0.001$ ), transition ( $h^* = 0.008$ ,  $W = 0.007$ ), and sedimentation ( $h^* = 0.008$ ,  $W = 0.007$ ) zones presented in Fig. 9. For each case, the number of particles deposited inside the channel corresponds to the percentage of sedimented particles.

As illustrated in Table 2, the percentage of sedimented particles found numerically for each case corresponds well to the regimes predicted by the regime diagram and thus confirms the validity of the approach.

**Table 2**

Percentages of sedimented particles in a straight channel for configurations corresponding respectively to the transport regime ( $h^* = 0.008$ ,  $W = 0.001$ ), the transition regime ( $h^* = 0.008$ ,  $W = 0.0035$ ), and the sedimentation regime ( $h^* = 0.008$ ,  $W = 0.0075$ ) presented in Fig. 9. Comparison between the regime diagram predictions (Fig. 9) and particle tracking numerical simulations results.

$(h^*, W)$	$\frac{W}{h^*}$	% of sedimented particles	
		Numerical experiment	Diagram prediction
(0.008, 0.001)	0.125	21	<25 (Transport)
(0.008, 0.0035)	0.437	43	∈ [25, 75] (Transition)
(0.008, 0.0075)	0.937	80	>75 (Sedimentation)

#### 4.2. Wavy channel with sinusoidal walls

The channel is here defined by the following dimensionless parameters: the average corrugation amplitude  $\delta_0 = \frac{A_0}{H_0} = \frac{A_1+A_2}{2H_0}$ , the phase shift  $\alpha = \frac{2\pi \Delta X}{L_0}$ , the asymmetry between the wall corrugations  $\gamma = \frac{A_2-A_1}{A_1+A_2}$  and  $l^* = \frac{L_0}{L_\infty}$ . In this case,  $h^* = \epsilon l^*$ .

The study for this type of channel is slightly more complex than for straight channels because three additional geometrical parameters need to be taken into account ( $\delta_0$ ,  $\alpha$ ,  $\gamma$ ). To do so, we first rewrote Eq. (9) as a function of these parameters. Then, we applied the criteria defining the three transport regimes using this equation. The strategy is to vary one parameter and keep the other two constant each time to investigate the parameter's influence on the regimes diagram.

The main emerging result is that, whatever the walls amplitudes and horizontal shift are, the variations of  $W_{cr1}$  and  $W_{cr2}$  as functions of  $h^*$  remain linear. Therefore, even for channels with sinusoidal walls, the diagram is similar to the one obtained for straight channels (Fig. 9). The difference lies in the extension or reduction of the transport and sedimentation zones depending on the channel geometry. In order to assess the influence of the channel geometry on the regime diagram, we studied three main configurations:

- channel having in phase walls ( $\alpha = 0$ ,  $\gamma \neq 0$ )
- channel having out of phase identical walls ( $\alpha \neq 0$ ,  $\gamma = 0$ )
- channel having walls with maximum phase lag ( $\alpha = \pi$ ,  $\gamma \neq 0$ )



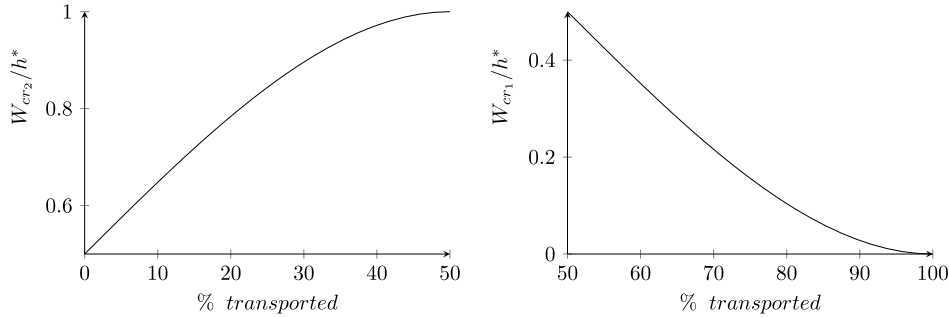


Fig. 10. Variation of  $W_{cr1}/h^*$  and  $W_{cr2}/h^*$  as a function of the percentage of particles transported inside the channel.

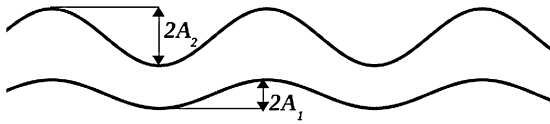


Fig. 11. Channel with in phase sinusoidal walls. Here, the upper wall is more corrugated than the lower wall.

#### 4.2.1. Channel with in phase walls

In this case, there is no horizontal shift  $\Delta X$  between the two walls and  $\alpha = 0$ . The two walls do not have necessarily the same amplitude (Fig. 11).

By varying the amplitudes of the walls  $A_1$  and  $A_2$ , the corrugations wavelength  $L_0$  and the channel aperture  $H_0$ , we find that in all cases,  $W_{cr1} = 0.156h^*$  and  $W_{cr2} = 0.84h^*$ . These values are identical to the ones obtained in Section 4.1. Consequently, the diagram obtained for straight channels (Fig. 9) can also be used to characterize transport regimes in wavy channels without horizontal shift between the walls. To verify this hypothesis, the numerical experiments presented in Section 4.1 were conducted in a channel with sinusoidal in phase walls using the same values of  $(h^*, W)$ . The percentages of sedimented particles found numerically are mentioned in Table 3.

Again, the percentages of sedimented particles agree well with the predictions of the regime diagram, confirming therefore the validity of the regime diagram for wavy channels with in phase walls. Interestingly, the diagram is identical to the one obtained for straight channels.

#### 4.2.2. Channel with out of phase identical walls

In this case, the two walls are identical, i.e. they have the same corrugation amplitude  $A_1 = A_2$  and thus  $\gamma = 0$ .  $\alpha$  and  $\delta_0$  can vary respectively such as:

- $\delta_0$  will be modified by changing the walls amplitude and/or the channel mean aperture.
- $\alpha$  will be modified by changing the phase lag between the upper wall and the lower wall.  $\alpha = 0$  corresponds to channels with parallel walls and  $\alpha = \pi$  corresponds to channels with mirror-symmetrical walls

##### a. Influence of $\delta_0$

Let us consider  $W_{cr1} = c_1 h^*$  and  $W_{cr2} = c_2 h^*$  with  $c_1$  and  $c_2$  two constants describing their linear variation. The variations of  $c_1$  and  $c_2$  as functions of  $\delta_0$  are plotted in Fig. 12. When  $\delta_0$  increases,  $c_1$  increases as well, which means that the transport zone increases. Conversely,  $c_2$  decreases when  $\delta_0$  increases, leading to a decrease of the sedimentation zone.

To further illustrate these variations, we compared two different cases considering  $\delta$  equal respectively to 0.1 and 0.4 while

keeping  $\alpha = \pi$  constant and plotted the associated regimes on the same diagram (Fig. 13). One can see that increasing the corrugation amplitude (by increasing  $\delta_0$ ) leads to an increase of both the transport and sedimentation zones.

Here again, the numerical experiments performed using 100 particles were conducted to verify the results. Two configurations corresponding to two pairs of  $(h^*, W)$  located respectively in the two variation zones of the diagram were used considering  $\delta_0 = 0.1$  and  $\delta_0 = 0.4$ . The results are mentioned in Table 4.

For  $(h^* = 0.01, W = 0.0021)$ , when  $\delta_0 = 0.1$ , the percentage of the deposited particles is equal to 30% (transition), while this percentage is equal to 10% when  $\delta_0 = 0.4$  (transport). For  $(h^* = 0.01, W = 0.0074)$ , when  $\delta_0 = 0.1$ , the percentage of the sedimented particles is equal to 70% (transition), while this percentage is equal to 80% when  $\delta_0 = 0.4$  (sedimentation). The numerical experiments confirm then the effect of  $\delta_0$  on the regime diagram.

##### b. Influence of $\alpha$

To investigate the effect of the phase lag between the walls on particle transport,  $\alpha$  was varied from 0 to  $2\pi$  for two cases:  $\delta_0 = 0.1$  and  $\delta_0 = 0.2$ . The variation of  $c_1$  and  $c_2$  as a function of  $\alpha$  is plotted in Fig. 14.

Firstly, one can see that the behavior of the particles does not change when the phase lag between the walls is in the opposite direction ( $\pm \alpha$ ). For example, if the lower wall is shifted from the upper wall by  $\Delta X = L_0/4$  ( $\alpha = \pi/2$ ), the particles settle at the same distance as if the shift was  $\Delta X = -L_0/4$  ( $\alpha = 3\pi/2$ ) (Fig. 15).

Secondly,  $c_1$  reaches its maximal value when the phase lag between the walls is maximum ( $\alpha = \pi$ ) which means that the transport zone increases with the increase of the phase lag. Similarly,  $c_2$  is minimum for  $\alpha = \pi$  and therefore the sedimentation zone also increases with the increase of the phase lag.

To further illustrate these variations, we compared two different cases considering  $\alpha$  equal respectively to 0 and  $\pi$  while keeping  $\delta = 0.2$  constant and plotted the associated regimes on the same diagram (Fig. 16). One can see that increasing the phase lag between the walls leads to an increase of both the transport and sedimentation zones in the diagram, their maximum extents being reached when the channel walls are mirror symmetric ( $\alpha = \pi$ ).

Here again, the numerical experiments performed using 100 particles were conducted to verify the results. Two configurations corresponding to two pairs of  $(h^*, W)$  located respectively in the two variation zones of the diagram were used considering  $\alpha = 0$  and  $\alpha = \pi$ . The results are mentioned in Table 5.

It is shown that for  $(h^* = 0.009, W = 0.0016)$ , when  $\alpha = 0$ , the percentage of the deposited particles is equal to 26% (transition), while this percentage is equal to 20% when  $\alpha = \pi$  (transport). For  $(h^* = 0.0085, W = 0.0065)$ , when  $\alpha = 0$  the percentage of the sedimented particles is 66% (transition), while this percentage is 80% when  $\alpha = \pi$  (sedimentation). The effect of  $\alpha$  on the regime diagram is again confirmed by the numerical experiment.

**Table 3**

Percentages of sedimented particles in a sinusoidal channel with in phase walls for configurations corresponding respectively to the transport regime ( $h^* = 0.008$ ,  $W = 0.001$ ), the transition regime ( $h^* = 0.008$ ,  $W = 0.0035$ ), and the sedimentation regime ( $h^* = 0.008$ ,  $W = 0.0075$ ) presented in Fig. 9. Comparison between the regime diagram predictions (Fig. 9) and particle tracking numerical simulations results.

$(h^*, W)$	$\frac{W}{h^*}$	% of sedimented particles	
		Numerical experiment	Diagram prediction
(0.008, 0.001)	0.125	22	<25 (Transport)
(0.008, 0.0035)	0.437	44	$\in [25, 75]$ (Transition)
(0.008, 0.0075)	0.937	79	>75 (Sedimentation)

**Table 4**

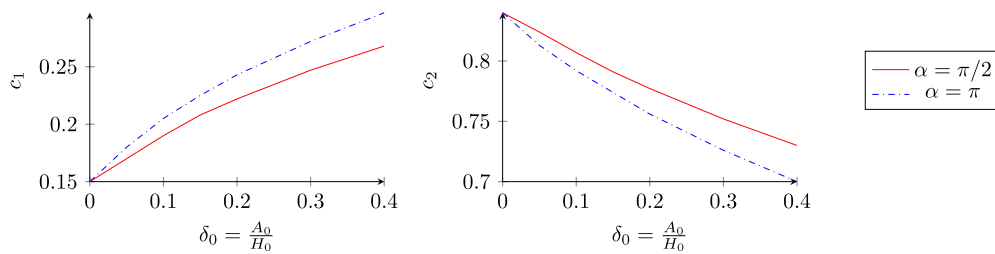
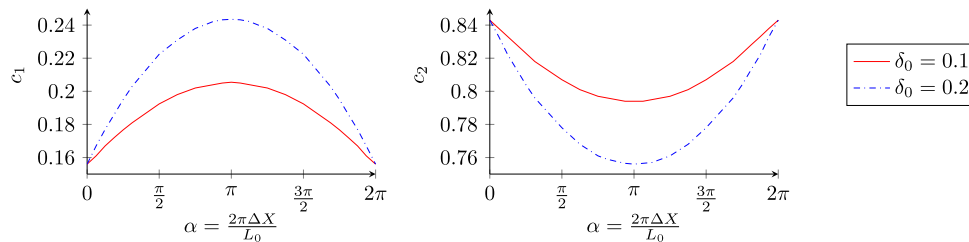
Percentages of sedimented particles in sinusoidal channels with out of phase identical walls defined respectively by  $\delta_0 = 0.1$  and  $\delta_0 = 0.4$ , for two configurations corresponding to ( $h^* = 0.01$ ,  $W = 0.0021$ ) and ( $h^* = 0.01$ ,  $W = 0.0074$ ). Comparison between the regime diagram predictions (Fig. 13) and particle tracking numerical simulations results.

$(h^*, W)$	$\frac{W}{h^*}$	$\delta_0$	% of sedimented particles	
			Numerical experiment	Diagram prediction
(0.01, 0.0021)	0.21	0.1	30	$\in [25, 75]$ (Transition)
		0.4	10	<25 (Transport)
(0.01, 0.0074)	0.74	0.1	70	$\in [25, 75]$ (Transition)
		0.4	80	>75 (Sedimentation)

**Table 5**

Percentages of sedimented particles in sinusoidal channels with out of phase identical walls defined respectively by  $\alpha = 0$  and  $\alpha = \pi$ , for two configurations corresponding to ( $h^* = 0.009$ ,  $W = 0.0016$ ) and ( $h^* = 0.0085$ ,  $W = 0.0065$ ). Comparison between the regime diagram predictions (Fig. 16) and particle tracking numerical simulations results.

$(h^*, W)$	$\frac{W}{h^*}$	$\alpha$	% of sedimented particles	
			Numerical experiment	Diagram prediction
(0.009, 0.0016)	0.177	0	26	$\in [25, 75]$ (Transition)
		$\pi$	20	<25 (Transport)
(0.0085, 0.0065)	0.764	0	66	$\in [25, 75]$ (Transition)
		$\pi$	80	>75 (Sedimentation)

**Fig. 12.** Variation of  $c_1$  (left) and  $c_2$  (right) as a function of  $\delta_0$  for two cases:  $\alpha = \pi/2$  and  $\alpha = \pi$ .**Fig. 14.** Variation of  $c_1$  (left) and  $c_2$  (right) as a function of  $\alpha$  for two cases:  $\delta = 0.1$  and  $\delta = 0.2$ .

#### 4.2.3. Channel with maximum phase lag between the walls

In this type of channel, the horizontal shift between the walls is maximum ( $\Delta X = L_0/2$  or  $\alpha = \pi$ ). When the two walls have the same corrugation amplitude ( $\gamma = 0$ ), the channel presents a mirror-symmetrical geometry (Fig. 17). When the walls are not identical,  $\gamma$  varies between  $-1$  when the upper wall is flat ( $A_2 = 0$ ) and  $1$  when the lower wall is flat ( $A_1 = 0$ ).  $\gamma < 0$  means that the lower wall is more corrugated than the upper wall and vice versa.

To assess the influence of the corrugation amplitude asymmetry on particle transport, we studied the variation of  $c_1$  and  $c_2$  as a function of  $\gamma$  for two different average corrugation amplitudes  $\delta_0 = 0.1$  and  $\delta_0 = 0.2$  (Fig. 18).

$c_1$  decreases when increasing  $\gamma$ , it is maximal when the upper wall is flat ( $\gamma = -1$ ) and minimal when the lower wall is flat ( $\gamma = 1$ ). This means that the transport zone in the diagram is maximal when the upper wall is flat. The transport zone decreases

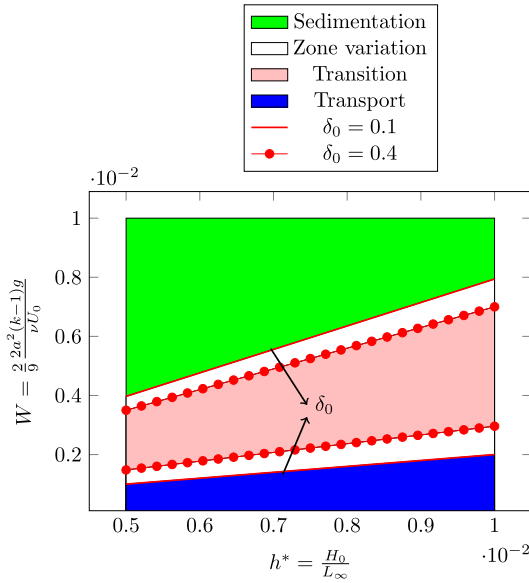


**Fig. 13.** Effect of increasing  $\delta_0$  on particle transport regimes for channels having out of phase identical walls. The red solid lines present the limits between the regimes for a channel with  $\delta_0 = 0.1$  and the red dotted lines present the limits between the regimes after increasing the walls corrugations ( $\delta_0 = 0.4$ ). The white zones present the variations in the transport and sedimentation zones respectively.

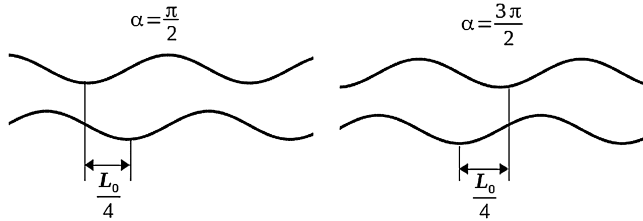


**Fig. 15.** Channel with sinusoidal walls with positive horizontal shift  $\alpha = \pi/2$  (left) and negative horizontal shift  $\alpha = 3\pi/2$  (right).

with increasing upper wall corrugation or decreasing lower wall corrugation, to become minimal when the lower wall is flat. However, when  $\gamma = 0.5 = \gamma_{cr1}$  (the upper wall corrugation is equal to three times the lower wall corrugation), the value of  $c_1$  is the same for the two values of  $\delta_0$ . Further calculations showed that for this case ( $\gamma = \gamma_{cr1}$ ),  $c_1$  is constant and independent of  $\delta_0$ . When  $\gamma < \gamma_{cr1}$ ,  $c_1$  increases with increasing  $\delta_0$  and, as a result, the transport zone increases.  $\gamma > \gamma_{cr1}$  leads to the opposite result.

$c_2$  also decreases when increasing  $\gamma$ . Similarly to what can be observed in the variation of  $c_1$ , when  $\gamma = -0.5 = \gamma_{cr2}$  (the lower wall corrugation is three times the upper wall corrugation), the value of  $c_2$  is constant and independent of  $\delta_0$ . When  $\gamma < \gamma_{cr2}$ ,  $c_2$  increases with increasing  $\delta_0$  and, as a result, the sedimentation zone increases. The opposite result appears for  $\gamma > \gamma_{cr2}$ .

To further illustrate these variations, we compared two different cases considering the  $\gamma$  equal respectively to 1 and  $-1$  while keeping  $\delta = 0.2$  constant and plotted the associated regimes on the same diagram (Fig. 19). For each case, the pair  $c_1, c_2$  are respectively equal to 0.11, 0.68 and 0.31, 0.88. One can see that increasing the upper wall corrugation relatively to the lower wall leads to a decrease of the transport zone and to an increase of the sedimentation zone in the regime diagram.

Here again, we verified the predictions of the regime diagram against the numerical experiment performed using 100 particles. Two configurations corresponding to two pairs of  $(h^*, W)$  located respectively in the two variation zones of the diagram were used

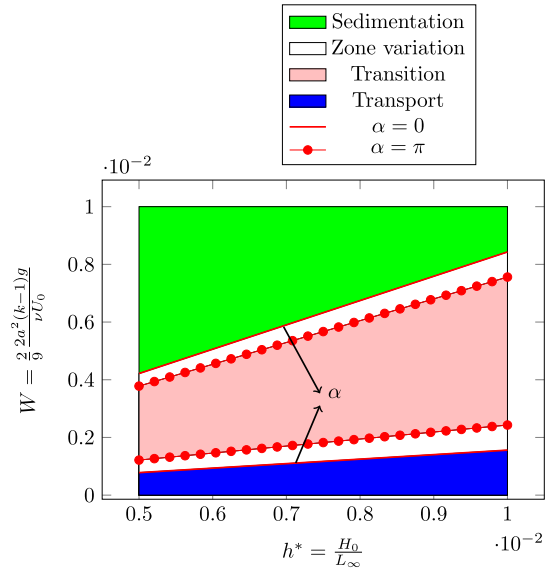


**Fig. 16.** Effect of increasing  $\alpha$  on particle transport regimes for channels having out of phase identical walls. The red solid lines present the limits between the regimes for a channel with  $\alpha = 0$  and the red dotted lines present the limits between the regimes after increasing the phase lag to  $\alpha_0 = \pi$ . The white zones present the variations in the transport and sedimentation zones respectively.

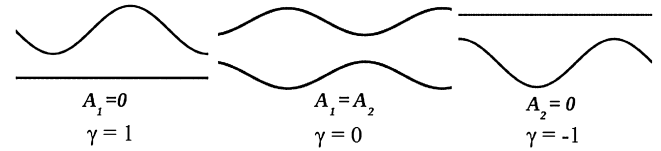


**Fig. 17.** Channels with lower flat wall (left), mirror-symmetrical walls (center) and upper flat wall (right).

considering  $\alpha = 0$  and  $\alpha = \pi$ . The results are mentioned in Table 6.

It is shown that for  $(h^* = 0.01, W = 0.001)$ , when  $\gamma = -1$ , no particles are deposited inside the channel (transport), while 30% of the particles are deposited when  $\gamma = 1$  (transition). For  $(h^* = 0.01, W = 0.0075)$ , when  $\gamma = -1$ , the percentage of the sedimented particles is equal to 53% (transition), while this percentage is equal to 80% when  $\gamma = 1$  (sedimentation). The effect of  $\gamma$  on the regime diagram by promoting sedimentation is once again verified by the numerical experiments.

#### 4.3. Summary

The behavior of weakly inertial particles injected in a channel laminar flow depends on the dimensionless number  $W$  and on the channel geometry. The separation between the transport, sedimentation and transition regimes is characterized by the linear variation of two critical values of  $W$ ,  $W_{cr1}$  and  $W_{cr2}$ . These two values are functions of the ratio between the aperture and the total length of the channel, which is characterized by the dimensionless number  $h^* = \frac{H_0}{L_\infty}$ .  $W_{cr1} = c_1 h^*$  defines the limit between the transport and transition zones, while  $W_{cr2} = c_2 h^*$  defines the limit between the transport and sedimentation zones. This separation leads to the definition of a regime diagram that is valid for arbitrary channel geometries.

It was found that the two different configurations of a straight channel and a channel with in phase sinusoidal walls ( $\alpha = 0$ ) share the same values of  $c_1$  and  $c_2$ . When the top and bottom walls are shifted, the direction of this shift does not affect the distance

**Table 6**

Percentages of sedimented particles in sinusoidal channels with out of phase identical walls defined respectively by  $\gamma = -1$  and  $\gamma = 1$ , for two configurations corresponding to  $(h^* = 0.01, W = 0.001)$  and  $(h^* = 0.01, W = 0.0075)$ . Comparison between the regime diagram predictions (Fig. 19) and particle tracking numerical simulations results.

$(h^*, W)$	$\frac{W}{h^*}$	$\gamma$	% of sedimented particles	
			Numerical experiment	Diagram prediction
(0.01, 0.001)	0.1	-1	0	<25 (Transport)
		1	30	$\in [25, 75]$ (Transition)
(0.01, 0.0075)	0.75	-1	53	$\in [25, 75]$ (Transition)
		1	80	>75 (Sedimentation)

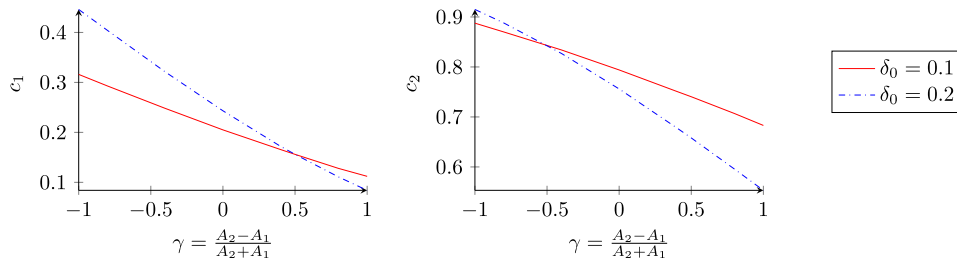


**Fig. 18.** Variation of  $c_1$  (left) and  $c_2$  (right) as a function of  $\gamma$  for two different average corrugation amplitudes  $\delta_0 = 0.1$  and  $\delta_0 = 0.2$ .

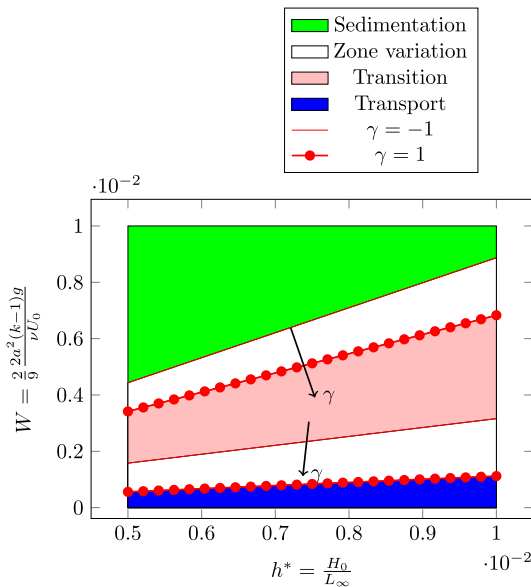


**Fig. 19.** Effect of inverting the asymmetry of wall corrugations amplitudes  $\gamma$  on particle transport regimes. The red solid lines present the limits between the regimes for a channel with a flat upper wall ( $\gamma = -1$ ) and the red dotted lines present the limits between the regimes for a channel with a flat lower wall ( $\gamma = 1$ ). The white zones present the variations in the transport and sedimentation zones respectively.

traveled by the particles. However, transport and sedimentation zones are optimum when the phase lag between the two walls is maximum ( $\alpha = \pi$ ).

In channels with two identical walls ( $\gamma = 0$ ), increasing the wall corrugation ( $\delta_0$ ) or the horizontal shift ( $\alpha$ ) tends to enlarge both the transport and sedimentation zones. In channels having nonidentical walls ( $\gamma \neq 0$ ) and a maximum phase lag ( $\alpha = \pi$ ), the increase of the upper wall corrugation compared to the lower wall one leads to a narrower transport zone and a larger sedimentation zone. The transport zone increases when the upper wall corrugation decreases, and reaches its maximum size when the upper wall becomes flat ( $\gamma = -1$ ). Conversely, increasing the upper wall corrugation promotes sedimentation, and the sedimentation

zone reaches its maximum area when the lower wall becomes flat ( $\gamma = 1$ ).

## 5. Conclusion

We present a study on the transport of particles with low inertia, in 2D closed channel flows. The flow is assumed to be laminar and dominated by viscous forces, characterized by low values of  $\epsilon Re_H$ ,  $\epsilon$  being the channel aspect ratio and  $Re_H$  the flow Reynolds number estimated on the channel mean aperture. Straight channels and wavy channels with sinusoidal walls are considered.

We show that when particle inertia is neglected, the particle behavior can be characterized by a dimensionless number  $W$  which represents the ratio between the particle settling velocity and the flow mean velocity. A differential equation defining the particle trajectory in wavy channels and an exact equation of this trajectory in straight channels were derived under the assumption that particle inertia can be neglected and that the flow velocity components can be explicitly calculated using the local cubic law. These equations were verified against numerical experiments based on a particle tracking technique using the particle motion equations together with the flow field obtained by solving Navier–Stokes equations. The numerical simulations were performed taking into account both particle and fluid inertias. The numerical results confirmed the assumptions under which the analytical approach was developed, and that the particle trajectory can be directly predicted according to the value of  $W$  and to the channel geometry without the need for further calculations or numerical simulations.

Based on these developments, a regime diagram was established, which predicts the transport or the sedimentation of particles as a function of  $W$  and of a geometrical parameter  $h^*$ , representing the ratio between the channel mean aperture and its total length. For channels with wavy walls, the regime diagram is similar to the one obtained for straight channels, but the zones of transport and sedimentation tend to increase or decrease depending on the channel geometry, related to the corrugation wavelength and amplitude and to the phase lag between the channel walls. It is shown that for a wavy channel having two in phase walls, the regime diagram is identical to the one obtained for a straight channel. When the two walls are out of phase, increasing the wall corrugation leads to an increase of the zones of transport and sedimentation in the diagram. Taking into account the asymmetry between the two walls corrugations, increasing the upper wall



corrugation relatively to the lower wall tends to decrease the transport zone and to increase the sedimentation zone. The regime diagram and the effects of the geometrical parameters on its zones variation were verified by numerical experiments which were conducted by releasing 100 particles in the channel and computing the percentages of particles that deposited inside the channel.

The results presented in this study describe in which way the geometry of a wavy channel affect the transport and the deposition of particles as well as the distance at which they will deposit inside the channel. It is believed that the proposed regime diagrams could help designing particle separation devices that can be of use in mineral processing or microfluidics and it may even give some insights into the transport of sediments in natural fractures.

An experimental verification is required as a next step and is currently undergoing. In addition, the analytical approach is being considered to extend to different flow regimes and to include other hydrodynamic forces on particles.

## References

- [1] M. Maxey, J. Riley, Equation of motion for a small rigid sphere in a nonuniform flow, *Phys. Fluids* (1958–1988) 26 (4) (1983) 883–889.
- [2] R. Gatignol, The Faxén formulas for a rigid particle in an unsteady non-uniform Stokes-flow, *J. Mec. Theor. Appl.* 2 (2) (1983) 143–160.
- [3] H. Stommel, Trajectories of small bodies sinking slowly through convection cells, *J. Mar. Res.* 8 (11) (1949) 24–29.
- [4] M. Maxey, The motion of small spherical particles in a cellular flow field, *Phys. Fluids* (1958–1988) 30 (7) (1987) 1915–1928.
- [5] L. Bergougnoux, G. Bouchet, D. Lopez, E. Guazzelli, The motion of solid spherical particles falling in a cellular flow field at low stokes number, *Phys. Fluids* (1994–Present) 26 (9) (2014) 093302.
- [6] A. Babiano, J. Cartwright, O. Piro, A. Provenzale, Dynamics of a small neutrally buoyant sphere in a fluid and targeting in Hamiltonian systems, *Phys. Rev. Lett.* 84 (25) (2000) 5764.
- [7] G. Haller, T. Sapsis, Where do inertial particles go in fluid flows? *Physica D* 237 (5) (2008) 573–583.
- [8] J. Cartwright, U. Feudel, G. Károlyi, A. de Moura, O. Piro, T. Tél, Dynamics of finite-size particles in chaotic fluid flows, in: *Nonlinear Dynamics and Chaos: Advances and Perspectives*, Springer, 2010, pp. 51–87.
- [9] E. Balkovsky, G. Falkovich, A. Fouxon, Intermittent distribution of inertial particles in turbulent flows, *Phys. Rev. Lett.* 86 (13) (2001) 2790.
- [10] M. Lunau, A. Lemke, O. Dellwig, M. Simon, Physical and biogeochemical controls of microaggregate dynamics in a tidally affected coastal ecosystem, *Limnol. Oceanogr.* 51 (2) (2006) 847–859.
- [11] R. Shaw, Particle-turbulence interactions in atmospheric clouds, *Annu. Rev. Fluid Mech.* 35 (1) (2003) 183–227.
- [12] J. Eaton, J. Fessler, Preferential concentration of particles by turbulence, *Int. J. Multiph. Flow.* 20 (1994) 169–209.
- [13] J. Bec, A. Silberberg, Fractal clustering of inertial particles in random flows, *Phys. Fluids* (1994–Present) 15 (11) (2003) L81–L84.
- [14] T. Nizkaya, J. Angilella, M. Buès, Inertial focusing of small particles in wavy channels: Asymptotic analysis at weak particle inertia, *Physica D* 268 (2014) 91–99.
- [15] J. Angilella, R. Vilela, A. Motter, Inertial particle trapping in an open vortical flow, *J. Fluid Mech.* 744 (2014) 183–216.
- [16] G. Segre, Radial particle displacements in Poiseuille flow of suspensions, *Nature* 189 (1961) 209–210.
- [17] J.A. Schonberg, E. Hinch, Inertial migration of a sphere in Poiseuille flow, *J. Fluid Mech.* 203 (1989) 517–524.
- [18] E.S. Asmolov, The inertial lift on a spherical particle in a plane Poiseuille flow at large channel Reynolds number, *J. Fluid Mech.* 381 (1999) 63–87.
- [19] A. Karnis, H. Goldsmith, S. Mason, The flow of suspensions through tubes: V. Inertial effects, *Can. J. Chem. Eng.* 44 (4) (1966) 181–193.
- [20] J. Matas, J. Morris, E. Guazzelli, Inertial migration of rigid spherical particles in Poiseuille flow, *J. Fluid Mech.* 515 (2004) 171–195.
- [21] J. Feng, H.H. Hu, D. Joseph, Direct simulation of initial value problems for the motion of solid bodies in a Newtonian fluid. Part 2. Couette and Poiseuille flows, *J. Fluid Mech.* 277 (1994) 271–301.
- [22] B. Yang, J. Wang, D. Joseph, H.H. Hu, T.-W. Pan, R. Glowinski, Migration of a sphere in tube flow, *J. Fluid Mech.* 540 (2005) 109–131.
- [23] D. Di Carlo, D. Irimia, R. Tompkins, M. Toner, Continuous inertial focusing, ordering, and separation of particles in microchannels, *Proc. Natl. Acad. Sci.* 104 (48) (2007) 18892–18897.
- [24] J. Martel, M. Toner, Inertial focusing in microfluidics, *Ann. Rev. Biomed. Eng.* 16 (2014) 371.
- [25] F. Bretherton, The motion of rigid particles in a shear flow at low Reynolds number, *J. Fluid Mech.* 14 (02) (1962) 284–304.
- [26] B. Ho, L. Leal, Inertial migration of rigid spheres in two-dimensional unidirectional flows, *J. Fluid Mech.* 65 (02) (1974) 365–400.
- [27] A. Jebakumar, K. Premnath, J. Abraham, Lattice Boltzmann method simulations of Stokes number effects on particle trajectories in a wall-bounded flow, *Comput. & Fluids* 124 (2016) 208–219.
- [28] R. Chen, W. Chen, C. Lai, Deposition of charged particles in a channel, *Powder Technol.* 74 (2) (1993) 135–140.
- [29] R. Chen, H. Chiou, D. Sun, Deposition of particles in a convergent channel, *Powder Technol.* 87 (1) (1996) 83–86.
- [30] T. Sapsis, G. Haller, Clustering criterion for inertial particles in two-dimensional time-periodic and three-dimensional steady flows, *Chaos* 20 (1) (2010) 017515.
- [31] R. Zimmerman, G. Bodvarsson, Hydraulic conductivity of rock fractures, *Transp. Porous Media* 23 (1) (1996) 1–30.
- [32] T. Auton, J. Hunt, M. Prud'Homme, The force exerted on a body in inviscid unsteady non-uniform rotational flow, *J. Fluid Mech.* 197 (1988) 241–257.
- [33] O. Druzhinin, L. Ostrovsky, The influence of Basset force on particle dynamics in two-dimensional flows, *Physica D* 76 (1) (1994) 34–43.
- [34] H. Faxén, Der Widerstand gegen die Bewegung einer starren Kugel in einer zähen Flüssigkeit, die zwischen zwei parallelen ebenen Wänden eingeschlossen ist, *Ann. Phys.* 373 (10) (1922) 89–119.
- [35] V.V. Mourzenko, J.-F. Thovert, P.M. Adler, Permeability of a single fracture: validity of the Reynolds equation, *J. Phys.* 5 (3) (1995) 465–482.
- [36] S. Sisavath, A. Al-Yaaruby, C.C. Pain, R.W. Zimmerman, A simple model for deviations from the cubic law for a fracture undergoing dilation or closure, *Pure Appl. Geophys.* 160 (5–6) (2003) 1009–1022.